

Water Resources Research

RESEARCH ARTICLE

10.1002/2016WR019128

Kev Points:

- A comprehensive pore-network model coupled with PHREEQC was developed to study microbially induced calcite precipitation in porous media
- Scale dependence of biogeochemical reaction rates was studied
- The possibility of reducing computational efforts by simplifying geochemical calculations was investigated

Supporting Information:

• Supporting Information S1

Correspondence to:

C.-Z. Qin, chaozhong.qin@gmail.com

Citation:

Qin, C.-Z., S. M. Hassanizadeh, and A. Ebigbo (2016), Pore-scale network modeling of microbially induced calcium carbonate precipitation: Insight into scale dependence of biogeochemical reaction rates, *Water Resour. Res.*, *52*, 8794–8810, doi:10.1002/2016WR019128.

Received 26 APR 2016 Accepted 24 OCT 2016 Accepted article online 1 NOV 2016 Published online 18 NOV 2016

Pore-scale network modeling of microbially induced calcium carbonate precipitation: Insight into scale dependence of biogeochemical reaction rates

Chao-Zhong Qin¹, S. Majid Hassanizadeh¹, and Anozie Ebigbo^{2,3}

¹Department of Earth Sciences, University of Utrecht, Utrecht, Netherlands, ²Department of Earth Science and Engineering, Imperial College, London, UK, ³Geothermal Energy and Geofluids Group, Institute of Geophysics, Department of Earth Sciences, ETH Zürich, Zürich, Switzerland

Abstract The engineering of microbially induced calcium carbonate precipitation (MICP) has attracted much attention in a number of applications, such as sealing of CO_2 leakage pathways, soil stabilization, and subsurface remediation of radionuclides and toxic metals. The goal of this work is to gain insight into pore-scale processes of MICP and scale dependence of biogeochemical reaction rates. This will help us develop efficient field-scale MICP models. In this work, we have developed a comprehensive pore-network model for MICP, with geochemical speciation calculated by the open-source PHREEQC module. A numerical pseudo-3-D micromodel as the computational domain was generated by a novel pore-network generation method. We modeled a three-stage process in the engineering of MICP including the growth of biofilm, the injection of calcium-rich medium, and the precipitation of calcium carbonate. A number of test cases were conducted to illustrate how calcite precipitation was influenced by different operating conditions. In addition, we studied the possibility of reducing the computational effort by simplifying geochemical calculations. Finally, the effect of mass transfer limitation of possible carbonate ions in a pore element on calcite precipitation was explored.

1. Introduction

Microbially induced calcium carbonate precipitation (MICP), particularly via the urea-hydrolysis pathway, has received much attention over the past years. As a novel subsurface engineering process, it is promising for a number of engineering applications [*De Muynck et al.*, 2010b; *Dhami et al.*, 2013; *Phillips et al.*, 2013], such as immobilization of groundwater contaminants [*Fujita et al.*, 2008], mitigation of wellbore leakage in geological carbon sequestration storage [*Cunningham et al.*, 2013, 2014], and soil condition improvement [*Ivanov and Chu*, 2008; *Cheng et al.*, 2013].

Regarding the engineering of MICP, the research has been mostly focused on targeting precipitation locations and reducing the cost of field applications [see *Cunningham et al.*, 2014]. Up to now, many lab-scale experiments have been performed to demonstrate controllable calcium carbonate precipitation [*Barkouki et al.*, 2011; *Ebigbo et al.*, 2012; *Mitchell et al.*, 2013; *Sham et al.*, 2013]. More recently, this has been successfully demonstrated also in field trials [*Cuthbert et al.*, 2013; *Cunningham et al.*, 2014; *Phillips et al.*, 2016].

In MICP, complex biogeochemical and hydrodynamics processes are involved [Al Qabany et al., 2012; Fauriel and Laloui, 2012; Hommel et al., 2013, 2015a, 2015b]. They may include ureolysis kinetics, multicomponent and microorganism transport, biofilm growth, equilibrium and kinetic geochemical reactions, calcite precipitation/dissolution, and porous structure evolution. The interplay of these processes determines the performance of MICP engineering. Due to this complexity, numerical modeling has been playing an important role in understanding the MICP processes as well as predesigning lab and field experiments. Several continuum-scale MICP models have been developed in the past. They varied in complexity and model assumptions. Martinez et al. [2014] presented a simple model to simulate the MICP in their column experiments. A good match was obtained by properly fitting the spatial distribution of immobile urease enzyme. Cuthbert et al. [2013] developed a two-dimensional model which coupled flow and transport of bacterial and reactive solute. However, the geochemistry was considerably simplified. The calcite precipitation rate was assumed to be stoichiometric to the ureolysis rate. Thus, information on pH was not available. Ebigbo

© 2016. American Geophysical Union. All Rights Reserved. et al. [2012] developed a complex MICP model considering most biogeochemical processes and hydrodynamics as mentioned above. They calibrated and verified the model against their sand column experiments. Later on, Hommel et al. [2015a] further improved the model of Ebigbo et al. [2012] by employing an updated ureolysis rate equation. The new ureolysis rate was fitted for a system of suspended cells of Sporosarcina pasteurii [Lauchnor et al., 2015]. They performed a comprehensive sensitivity analysis and showed that calcite precipitation was most sensitive to the ureolysis rate and the attachment of biomass.

Continuum-scale models are popular, because they have the potential to be used in field applications [*Brovelli et al.*, 2009; *Ebigbo et al.*, 2010; *Zhou*, 2015]. However, the performance of a continuum-scale model depends among other things on the determination of several material properties such as capillary pressure saturation relationship and relative permeability [*Hassanizadeh and Gray*, 1990; *Qin and Hassanizadeh*, 2014]. In the context of MICP, for instance, the constitutive relationship between reduced porosity and permeability is very important, particularly for the evaluation of the performance of MICP. Also, there are a few kinetic reaction rates such as biofilm growth rate, ureolysis rate, and calcite precipitation rate, which may be scale-dependent due to various heterogeneities in porous media such as nonuniform distributions of microorganisms and pore structures [*Noiriel et al.*, 2012, 2015]. To determine whether these reaction rates, which are usually measured in well-mixed batch experiments, can be directly used in continuum-scale models, the pore-scale modeling and associated upscaling techniques can be very helpful [*Li et al.*, 2006, 2007; *Lichtner and Kang*, 2007; *Van Noorden et al.*, 2010; *Kim et al.*, 2011].

In general, there are two kinds of pore-scale models, namely, direct-simulation [Von Der Schulenburg et al., 2009; Kang et al., 2010; Deng et al., 2013] and pore-network models [Thullner and Baveye, 2008; Raoof et al., 2012; Nogues et al., 2013; Qin and Hassanizadeh, 2015b]. The basic idea of a pore-network model is as follows. First, the porous medium of interest is geometrically represented by a network of idealized pore elements, in which pore bodies are used to approximate large pore spaces while the narrow regions between large pore spaces are approximated by pore throats. Then, flow and transport equations are solved based on the simplified pore elements [Qin, 2015]. In comparison to direct simulations, the pore-network modeling is very computationally efficient. This allows us to model a large computational domain with a number of REVs (representative elementary volume) [Bear and Bachmat, 1991] for upscaling studies. In a pore-network model, thermodynamic quantities (e.g., species concentrations and pressure) are usually defined over each pore element. The assumption of small variation of quantities in a pore element needs to be made. Otherwise, pore-element-scale effective parameters need to be derived [Qin and Hassanizadeh, 2015a], probably by conducting direct simulations. At this point, the pore-network modeling serves as a bridge between direct numerical simulation and continuum-scale modeling. And, the present work contributes to the pore-network modeling of MICP processes.

There have been many pore-scale modeling studies of mineral precipitation and dissolution [Raoof et al., 2012; Yoon et al., 2012] or biofilm growth in porous media [Tang et al., 2013; Rosenzweig et al., 2014; Peszynska et al., 2015]. Yoon et al. [2012] simulated mixing-induced calcium carbonate precipitation and dissolution in a microfluidic device using the lattice Boltzmann method (LBM). Due to the computational effort, only a few two-dimensional pore spaces were modeled. Nogues et al. [2013] simulated carbonate precipitation and dissolution using a pore-network model. The size of the computational domain was equivalent to an REV size. Pintelon et al. [2012] investigated biofilm growth in a porous medium using the LBM. Most recently, Qin and Hassanizadeh [2015b] developed a pore-network model for solute transport and biofilm growth in a porous medium. A variable coefficient, which was shown to be a function of biofilm volume fraction and Damköhler number, was used to account for the nonequilibrium mass exchange between aqueous phase and biofilm.

To the best of our knowledge, there are few pore-scale modeling studies of MICP [Zhang and Klapper, 2010, 2014], particularly for a large domain of porous media. Thus, in this work, in light of the computational efficiency of pore-network modeling, we have developed a comprehensive pore-network model for MICP. It solves for flow and transport, biofilm growth, calcium carbonate precipitation, and geochemistry. As a first attempt, we modeled a two-dimensional network structure with an extensive dimension in the flow direction, which is quite similar to a pseudo-3-D microfluidic device [Zhang et al., 2010]. The objective of this work is to investigate pore-scale processes of MICP. Particularly, we studied the scale dependence (i.e., from the pore-element scale to the REV scale) of biogeochemical reaction rates, which are very important for the development of a simplified continuum-scale model.

Table 1. Ureolysis and Geochemical Reactions Under Consideration ^a			
Reactions		$\log K_{eq}$	
Ureolysis Kinetic Equilibrium	$CO(NH_2)_2 + 2H_2O \rightarrow 2NH_3 + H_2CO_3$ $CaCO_3 \leftrightarrow Ca^{2+} + CO_3^{2-}$ $H_2O \leftrightarrow H^+ + OH^-$ $H_2CO_3 \leftrightarrow H^+ + HCO_3^-$ $HCO_3^- \leftrightarrow H^+ + CO_3^{2-}$ $NH_4^+ \leftrightarrow H^+ + NH_3$ $CaHCO_3^+ \leftrightarrow Ca^{2+} + CO_3^{2-} + H^+$ $Ca^{2+} + H_2O \leftrightarrow CaOH^+ + H^+$	-8.48 -14 -6.35 -10.329 -9.252 -11.435 -12.78	

 $^{\rm a}$ Equilibrium constants were given at 25 $^{\circ}$ C [Parkhurst and Appelo, 2013].

2. Model Development

2.1. Transport and Biogeochemical Processes in MICP

The bacterial strain *Sporosarcina pasteurii* produces large amounts of urease [*Bachmeier et al.*, 2002]. Urea is hydrolyzed by the enzyme urease in the biomass, which generates ammonia and carbonate acid. The subsequent protonation of ammonia to ammonium causes the increase of pH value. This dramatically increases the availability of carbonate ions leading to the precipitation of calcium

carbonate (i.e., calcite). Throughout the paper, we do not distinguish calcium carbonate from calcite, because several XRD measurements have confirmed that calcite is the predominant polymorph in MICP [Lauchnor et al., 2013; Phillips et al., 2015]. Table 1 lists the relevant ureolysis, as well as kinetic and equilibrium geochemical reactions. All equilibrium constants are given at 25° [Parkhurst and Appelo, 2013]. Biomass grows in the presence of nutrient and oxygen (the electron acceptor) following double Monod kinetics (see equation (6)). In this work, we considered saturated water flow in the porous medium. Biomass, urea, nutrient, oxygen, and geochemical components (e.g., total C, N, and Ca) were transported under advection and diffusion. Suspended biomass was assumed to interact with immobile biofilm by attachment and detachment. The pore structure was updated based on biofilm growth and calcite precipitation. More detail can be found in sections 2.3 and 2.4.

2.2. Pore Network Generation

We have developed a novel pore-network generator. The generation algorithm is briefly described as follows. First, predefined pore bodies are randomly filled into a given computational domain without overlapping. Then, pore throats are generated by constructing triangles for a two-dimensional domain or tetrahedra for a three-dimensional domain among all pore bodies. Third, an elimination process is applied to the generated pore throats in order to reach an average coordination number [Raoof and Majid Hassanizadeh, 2010]. Finally, a search is conducted to find all isolated pore bodies and clusters. These are marked and deleted from the network.

For the case studies in this work, we calibrated the generated pore network to represent the packed sand porous media used by *Ebigbo et al.* [2012]. The pore network dimension is 112 mm in the flow direction (see Figure 1a). Typically, the REV size of a homogeneous porous medium should be at least as large as 15–20 grain particles size in each direction, such that obtained material properties (e.g., porosity and permeability) do not change by further increasing of the size of the average domain. In our work, we defined the REV size of 15 and 10 mm along the x and y directions, respectively. This allows us to study the effect of flow conditions on REV-scale calcite distributions. On the other hand, to reduce the computational effort, only one layer of pore elements in the z direction were considered. A truncated lognormal distribution was assumed for pore body sizes. The size of a pore throat was determined by the sizes of its neighboring pore bodies. Figure 1b shows the distributions of pore body size, pore throat size, pore throat length, and coordination number. The generated network has a porosity of 0.37, and permeability of 1.6×10^{-10} m². More detail of the geometrical properties of the pore network can be found in Table 2.

2.3. Governing Equations

Table 3 lists the governing equations implemented in the pore-network model. They describe saturated water flow, general species transport, suspended biomass transport, as well as biofilm and calcite evolutions. In the following, we primarily explain the notions in these equations. For more detail, one can refer to *Qin and Hassanizadeh* [2015b].

First, we solved Hagen-Poiseuille based volume balance equation of water to obtain pressure field and pore-throat fluxes. In equation (1) (see Table 3), Q_{ij} [L³/T] is the volumetric flow rate of water from pore body i to j, G_{ij} [L⁵T/M] is the conductance of pore throat ij given by Appendix A1 in Supporting Information, p [M/LT²] is the water pressure in a pore body, N_i is the number of pore throats connected to pore body i,

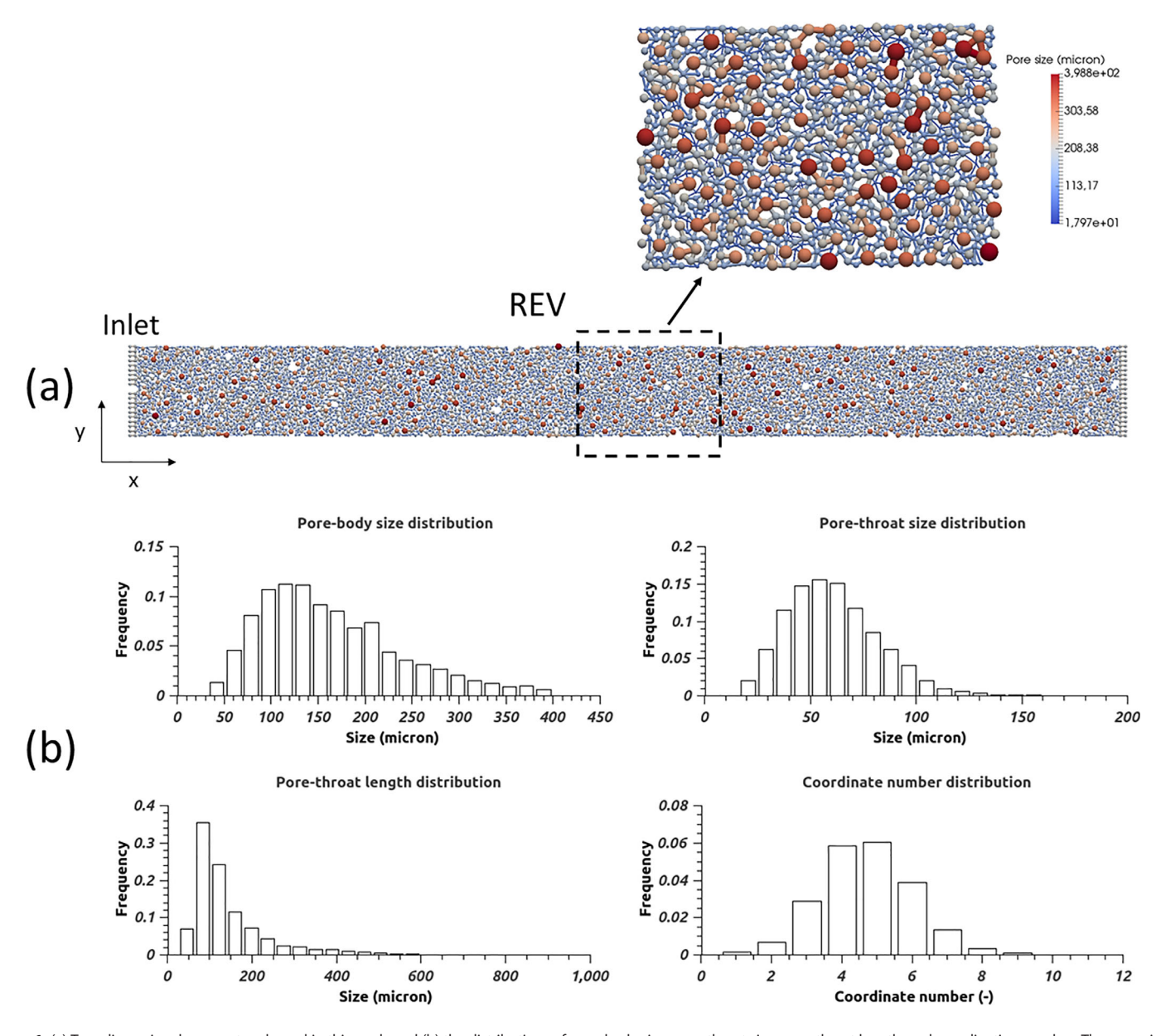


Figure 1. (a) Two-dimensional pore network used in this work; and (b) the distributions of pore-body size, pore-throat size, pore-throat length, and coordination number. The zoom-in pore structure of an REV is schematically shown in Figure 1a.

and L_{ij} [L] is the pore-throat length. Next, equations (2a) and (2b) for the mass conservations of urea, nutrient, oxygen, and all geochemical components (i.e., charge balance, total hydrogen, total oxygen, total car-

Table 2. Geometric Information of the Pore Network Used in This Work			
Network Dimensions (x/y/z) ^a	112/10/0.5 mm		
Number of pore bodies/pore throats	5968/14057		
Minimum, maximum, and mean sizes of pore body	30/400/150 μm		
Porosity ^b	0.37		
Permeability ^b	$1.6 \times 10^{-10} \mathrm{m}^2$		
Average coordinate number	4.7 (estimated)		

 $^{^{\}rm a}$ One layer of pore elements in the z direction are considered. The layer thickness is 0.5 mm.

bon, total nitrogen, total calcium, total sodium, and total chlorine) were solved to obtain their concentrations in each pore body and pore throat, respectively. These species can be present in both water phase and biofilm. For simplicity, we assumed the mass equilibrium of species between water phase and biofilm in each pore element such that there is equal concentration in both phases. Note that unlike the mixing-induced bioreaction [*Acharya et al.*, 2007],

^bThe generated network approximates the packing sand column from *Ebigbo et al.* [2012].

nutrient and oxygen are premixed before injected into the system in MICP. Therefore, the equilibrium assumption is probably acceptable for small biofilm content and small ureolysis rate considered in this work [*Qin and Hassanizadeh*, 2015a]. And, this needs to be further confirmed by direct simulations. In equations (2a) and (2b), the superscript m denotes the species, C is the species mass/molar concentration, ε^c is the calcite volume fraction, V_i^o [L³] is the original volume of pore body in the absence of calcite and biofilm, D_{ij}^w and D_{ij}^f [L²/T] are the species dispersion coefficients in water phase and biofilm, respectively, A_{ij}^w and A_{ij}^w [L²] are the cross-sectional areas of water phase and biofilm in the pore throat, and R is the sink/source term. Third, equations (3a) and (3b) for the transport of suspended biomass were solved to obtain its concentrations in each pore body and pore throat, respectively. ε^w is the volume fraction of water phase defined by 1 $-\varepsilon^c - \varepsilon^f$ (ε^f is the volume fraction of biofilm). The difference from the species transport equations is that suspended biomass only exists in water phase. Finally, the biofilm and calcite volume fractions in each pore element were updated by solving equation (4). The superscript s denotes the immobile solid phases, and ρ [M/L³] is the density.

2.4. Constitutive Relations

To supplement the governing equations given in section 2.3, a number of constitutive relations need to be provided. They include biomass and biofilm evolutions, bioreactions, calcium carbonate precipitation/dissolution, ureolysis, and source/sink terms for geochemical components. Usually, these relationships are scale-dependent. In the following, we present individual constitutive equations which were derived at the pore-element scale. Also, all geometrical relationships used by the pore-network model are given by Appendix A in Supporting Information.

2.4.1. Suspended Biomass and Biofilm

The source/sink term for suspended biomass in equations (3a) and (3b) is assumed to be given by the following equation:

$$R^{bio} = \underbrace{\mu \varepsilon^{w} C^{bio}}_{growth} - \underbrace{k_{dec,1} \left(1 + \frac{m_{H^{+}}^{2}}{K_{pH}}\right) \varepsilon^{w} C^{bio}}_{decay} - \underbrace{k_{att} S^{bio} C^{bio}}_{attachment} + \underbrace{\left\{\frac{(k_{det,1} + k_{det,2} \mu) \rho^{f} \varepsilon^{w}}{\varepsilon^{f} + \varepsilon^{c}} \frac{\mathcal{E}^{f}}{K_{ij}} (in \ pore \ throat)}_{0 \ (in \ pore \ body)}\right.}_{detachment}.$$
(5

Several mechanisms contribute to source or sink of the suspended biomass [see *Ebigbo et al.*, 2012]. In equation (5), on the right-hand side, the first term denotes the growth of biomass; the second term is the decay of biomass with the pH effect taken into account; the third term shows the first-order kinetics of biomass attachment; the last term denotes the detachment of biofilm due to the water shear force [*Qin and Hassanizadeh*, 2015b]. The detachment of biofilm in a pore body was neglected due to the relatively small pore velocity. The subscripts i/ij are omitted unless it is necessary.

In equation (5), m_{H^+} is the molality of proton, K_{pH} is an empirical constant, $k_{dec,1}$ is the endogenous decay rate constant, k_{att} is the attachment coefficient, S^{bio} is the available specific area for biomass attachment in a pore element, $k_{det,1}$ is the detachment rate constant due to the water shear force, $k_{det,2}$ is the second detachment rate constant due to the biofilm growth, and μ is the growth rate coefficient given by double-Monod kinetics [Cunningham and Mendoza-Sanchez, 2006]

$$\mu = k_{\mu} \frac{C^{n}}{K_{n} + C^{n}} \frac{C^{o}}{K_{n} + C^{o}},\tag{6}$$

where k_{μ} is the maximum substrate utilization rate constant, C^n and C^o are the mass concentrations of nutrient and oxygen, respectively, and K_n and K_o are the half saturation constants.

The source/sink term for biofilm in equation (4) is given as

$$R^{f} = \underbrace{\mu \varepsilon^{f} \rho^{f}}_{growth} - \underbrace{\left(k_{dec,1} + k_{dec,2} \frac{\max\left(-r_{prec/diss}, 0\right) M^{c}}{\rho^{c}(1 - \varepsilon^{c})}\right) \varepsilon^{w} \rho^{f}}_{decay} + \underbrace{k_{att} S^{bio} C^{bio}}_{attachment} - \underbrace{\left(k_{det,1} + k_{det,2} \mu\right) \rho^{f} \varepsilon^{w} \frac{\varepsilon^{f}}{\varepsilon^{f} + \varepsilon^{c}} \frac{Q_{ij}}{K_{ij}}}_{detachment}, (7)$$

where ρ^f is the biofilm density, $k_{dec,2}$ is the second decay rate constant due to the calcite precipitation [De Muynck et al., 2010a; Ebigbo et al., 2012], ρ^c is the calcite density, M^c is the molecular weight of calcite, and $r_{prec/diss}$ is the calcite precipitation/dissolution rate that is specified later.

2.4.2. Bioreactions for Nutrient and Oxygen

The consumptions of nutrient and oxygen in equations (2a) and (2b) are modeled by

$$R^{n} = -\frac{\mu}{V} \left(\rho^{f} \varepsilon^{f} + \varepsilon^{w} C^{bio} \right), \tag{8a}$$

$$R^{o} = F \times R^{n}$$
, (8b)

where Y is the yield coefficient and F denotes the mass of oxygen consumed per unit mass of nutrient.

2.4.3. Calcium Carbonate Precipitation and Dissolution

The calcium carbonate precipitation/dissolution rate was slightly revised based on the equation given by *Chou et al.* [1989]. Compared to other types of minerals, like anorthite and kaolinite, the calcite precipitation is much faster. As a result, the mass transfer limitation of reactive species (e.g., carbonate ion) may prevail in a pore element, particularly for sandy porous media whose pore spaces are relatively large. To take into account the effects of possible mass transfer limitation and complex nucleation mechanism on calcite precipitation rate at the pore-element scale [*Noiriel et al.*, 2012], we simply introduced a constant correction coefficient β . It is worth noting that in reality, this correction coefficient may be very variable depending on local pore morphology. On the other hand, if ureolysis rate is much slower than calcite precipitation rate, the selection of β value has minor effect on the predicted calcite precipitation. This will be shown in section 4.4. Here the equation for calcite precipitation/dissolution rate reads

$$r_{prec/diss} = \beta \left(k_1 a^{H^+} + k_2 a^{H_2 CO_3} + k_3 \right) \left(1 - \frac{a^{Ca^{2+}} a^{CO_3^{2-}}}{K_{sp}} \right)^{n_p} S^c, \tag{9}$$

where k_1 , k_2 , and k_3 are the reaction rate constants, a is the species activity, K_{sp} is the solubility of product of calcite, n_p is an empirical parameter, and S^c is the available specific area for calcite precipitation in a pore element. Therefore, the source/sink term for calcite phase is given as

$$R^{c} = -r_{prec/diss}M^{c}, (10)$$

where M^c is the molecular weight of calcite.

2.4.4. Ureolysis and Geochemistry

The revised ureolysis kinetics by *Lauchnor et al.* [2015] was used in this work. It takes into account additional mass transfer processes of reactants and products across the cell wall and regulatory processes within the cells. It is suitable to our pore-network model. The form of ureolysis was derived by fitting the Michaelis-Menten kinetics as [*Hommel et al.*, 2015a]

$$R^{u} = k_{urea}k_{ub}\rho^{f}\varepsilon^{f}\frac{m^{u}}{K_{u} + m^{u}},$$
(11)

where k_{urea} is the maximum activity of urease, k_{ub} is the mass ratio of urease to biofilm, m^u is the urea molality, and K_u is the half saturation constant for urea.

Finally, according to biogeochemical reactions shown in Table 1, the source/sink terms for individual geochemical components are given as follows:

For the total hydrogen:
$$R^H = 4 \times R^u$$
, (12a)

For the total oxygen:
$$R^0 = R^u + 3 \times r_{prec/diss}$$
, (12b)

For the total carbon:
$$R^C = R^u + r_{prec/diss}$$
, (12c)

For the total nitrogen:
$$R^N = 2 \times R^u$$
, (12d)

For the total calcium:
$$R^{Ca} = r_{prec/diss}$$
. (12e)

2.5. Numerical Implementation

Twelve species transport equations were solved in the pore-network model. They include urea (mol/L), nutrient (g/L), oxygen (g/L), suspended biomass (g/L), charge balance (mol/L), HT (total hydrogen, mol/L), OT (total oxygen, mol/L), CT (total carbon, mol/L), NT (total nitrogen, mol/L), CaT (total calcium, mol/L), NaT (total sodium, mol/L), and CIT (total chlorine, mol/L). In the developed MICP model, we distinguish dissolved oxygen molecules in the water with its consumption rate given by equation (8b) from bonded oxygen atoms in geochemical compounds (see Table 1). The two forms of oxygen do not interact with each other; and both mass conservation equations were solved. In the modeling, the chloride and sodium were introduced into the system during the injection of calcium-rich medium (i.e., CaCl₂ solution). The sequential non-iterative approach was used for the mixed kinetic-equilibrium system [Steefel et al., 2005]. The verification and discretization scheme of a general species transport equation in our pore-network model were presented in *Qin and Hassanizadeh* [2015b]. To obtain all primary and secondary species concentrations at each time step, the geochemical speciation was conducted using the open source PHREEQC module [Charlton and Parkhurst, 2011].

The time step is determined by the following criterion [Qin and Hassanizadeh, 2015b]:

$$\Delta t = \min\left(\frac{V_{ij}^0 \varepsilon_{ij}^w}{|Q_{ij}|}, \frac{L_{ij}^2}{4D_{ii}^w}\right). \tag{13}$$

Note that we used the same diffusivity for all geochemical components in order to keep the charge balance [Li et al., 2006]. In the employed pore network (see Figure 1b), a few pore throats have such small lengths that the time step calculated by equation (13) was too small. Without losing numerical accuracy and to reduce the computational effort, we increased the basis time step by 10–100 times depending on applied operating conditions. Due to the slow biofilm growth and calcite precipitation, we updated the pressure field only every 20 time steps. Also, the geochemistry speciation calculation was conducted every 10–50 time steps depending on the calcite precipitation rate and flow conditions.

Finally, the implemented boundary conditions for different operating conditions studied in this work are as follows. For the flow field equation (1), at the inlet, we had three types of boundary conditions, namely, pressure inlet, flux inlet, and no-flow conditions; at the outlet, a constant water pressure was specified. For the species transport equations (2) and (3), at the inlet, constant concentrations were specified; at the outlet, zero concentration gradient was imposed. Also, if the system was closed, zero concentration gradients were specified at the inlet.

3. Description of Test Cases

With the developed pore-network model, we studied a typical three-stage process in the engineering of MICP [Ebigbo et al., 2012; Hommel et al., 2015a], namely, injection of growth media for microorganisms, injection of calcium-rich media, and a period of calcite precipitation (with the system closed). In column experiments [e.g., Ebigbo et al., 2012], the process was usually repeated many times for achieving certain amount of precipitated calcite. In this work, we focused on the first cycle. Stage 1 lasts for 15 h, followed by stage 2 which lasts for the time of two pore volumes. Finally, stage 3 lasts for 4 h. It is noted that, in this

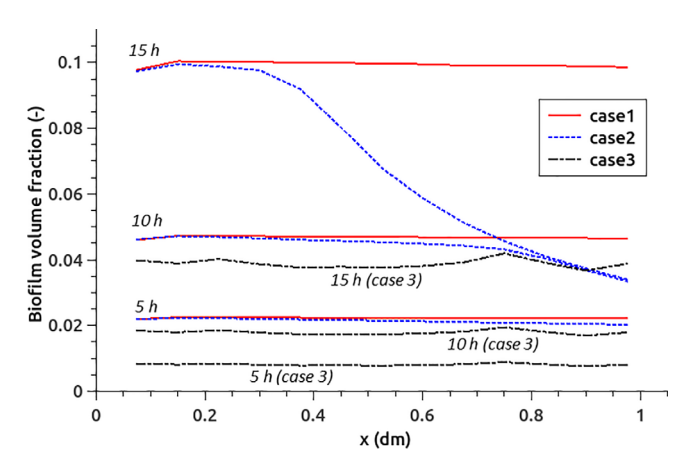


Figure 2. Distributions of REV-scale biofilm volume fraction at three instants (i.e., 5, 10, and 15 h) in case 1, case 2, and case 3 at stage 1. Case 1 and 3 have a flow rate of 1.88×10^{-2} ml/min, while case 2 has a lower flow rate of 3.76×10^{-3} ml/min.

work, stage 1 lasts for much longer time than other studies, in order to highlight the biofilm growth and the following calcite precipitation in a single three-stage process.

For the research objectives mentioned in section 1, a number of case studies were conducted. We basically set up three cases. Case 1 and case 2 were used to investigate the flow rate effect on MICP. In case 3, we assumed a patchy distribution of biofilm in the network to investigate this heterogeneity effect. Furthermore, for case 1, we varied the coefficient of β to check the effect of the mass transfer limitation of carbonate ions on the calcite

precipitation. Finally, we considered variants of case 1 and case 2 without complex geochemistry speciation. Instead, the calcite precipitation rate was assumed to be stoichiometric to the ureolysis rate. The aim is to determine under what conditions the MICP model can be simplified by dropping the calculation of geochemistry. All physical parameters used in the pore-network modeling are given in Table S1 of Supporting Information. Table S2 of Supporting Information lists the employed initial and boundary conditions for all case studies in this work.

4. Results and Discussion

Due to the lack of quantitative data on the interaction between biofilm growth and calcite precipitation in a pore element, in this work, we only modeled the first cycle of a three-stage injection strategy. As a result, in our case studies, the total amounts of biofilm and calcite in the system were relatively low. In this section, we present the results of biofilm and calcite distributions at the three stages. Focus is given to the discussion of scale dependences of biofilm growth rate, ureolysis rate, and calcite precipitation rate. In addition, we investigate whether the geochemistry speciation can be neglected when the calcite precipitation rate is limited by the concentration of carbonate ions.

4.1. Biofilm and Calcite Evolutions

The period of cell inoculation was not modeled [Sham et al., 2013]. Instead, in each case, an initial distribution of biofilm volume fraction was assumed to exist. In case 1 and case 2, the biofilm volume fraction was set to 0.01 initially in all pore bodies and pore throats. In case 3, randomly one third of pore elements had the initial volume fraction of 0.01; and the remaining pores were empty. This patchy distribution may be used to mimic natural formation of biofilm in the subsurface. To obtain a REV-scale quantity distribution along the flow direction, the average domain (i.e., the REV) was smoothly moved from the inlet to the outlet. Meanwhile, the REV-scale biofilm volume fraction was defined as $\bar{\epsilon}^f = \sum_{REV} V^0 \epsilon^f / \sum_{REV} V^0$. With the inlet boundary conditions of stage 1 given in Table S2 of Supporting Information, Figure 2 shows the distributions of REV-scale biofilm volume fraction at t = 5, 10, and 15 h in case 1, case 2, and case 3. It is seen that the distributions in case 1 and case 3 were uniform through the whole stage, which was due to the employed high flow rate. In case 2, the flow rate was reduced by 5 times as given in Table S2 of Supporting Information. Much less oxygen was delivered into the domain. At high biofilm volume fractions, most oxygen was consumed in the inlet region. Therefore, at the end of stage 1, the biofilm volume fraction decreased dramatically along the flow direction.

Biofilm evolution is a complex process which is determined by several mechanisms (see equation (7)). Different operating conditions may result in totally different pore-scale biofilm distributions, which correspond to different permeability-porosity relations at the macro scale. Figure 3 shows the distributions of pore-scale biofilm volume fraction at the end of stage 1 in the domain $0.4 \, \mathrm{dm} < x < 0.6 \, \mathrm{dm}$ for the three cases. Larger biofilm volume fraction was seen in a pore throat in comparison to the surrounding pore bodies. This is

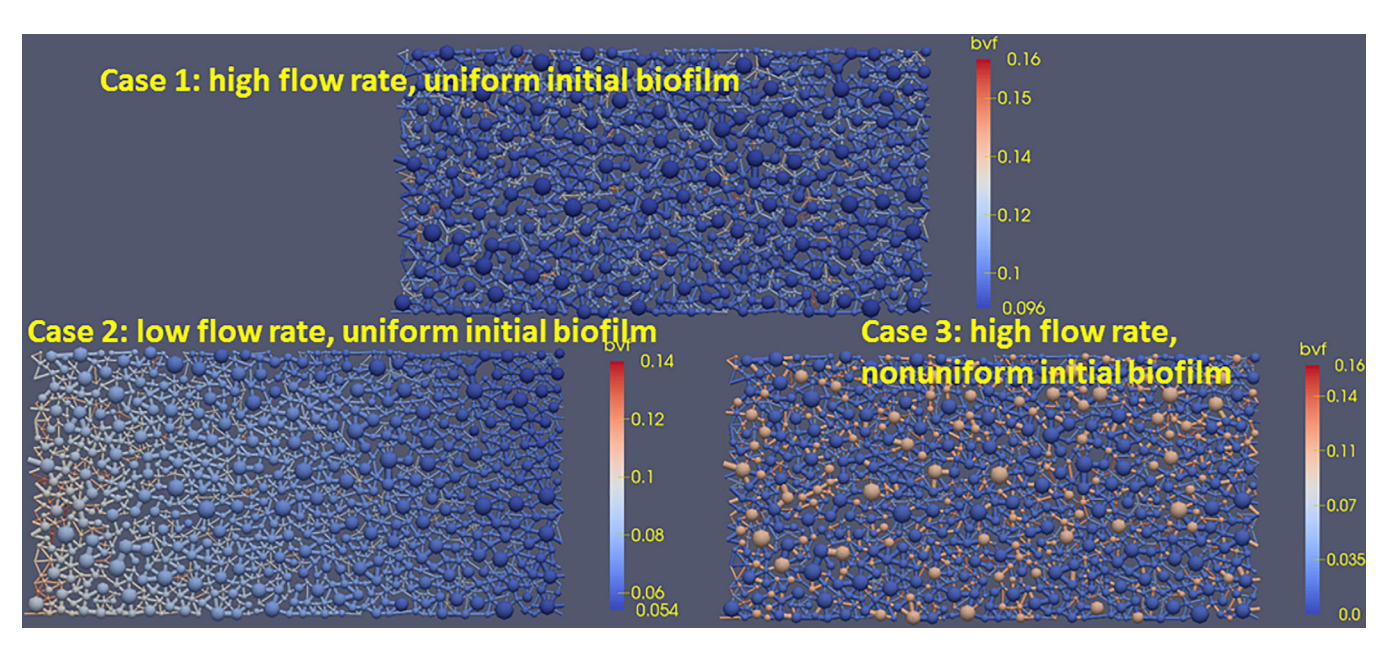


Figure 3. Distributions of pore-scale biofilm volume fraction (bvf) at the end of stage 1 in the domain of 0.4 dm < x < 0.6 dm in case 1, case 2, and case 3. For better visualization, the distribution for each case has its own color map range.

because the larger specific area of the pore throat resulted in more specific biomass attachment. Meanwhile, under the operating conditions used in this work, the biomass attachment rate was much larger than the detachment rate in a pore throat. In case 2, along the flow direction, a strong decrease of biofilm volume fraction was seen due to the limitation of oxygen availability. In case 3, the biofilm kept the patchy distribution. This is because biofilm growth needs initially attached biomass. Biofilm serves as the primary catalyst of hydrolysis of urea. It may determine the calcite precipitation locations and distributions. Therefore, predicting the distribution of biofilm is important in the modeling of MICP. The current challenges lie in the detachment mechanism of biofilm, and the subsequent transport of the detached biofilm [Kim and Fogler, 2000; Horn et al., 2003]. In our model, the biofilm detachment was simplified by a first-order kinetic model.

Figure 4a shows the distributions of REV-scale biofilm and calcite volume fractions in case 1, case 2, and case 3 at the end of stage 2. It was found that at the REV scale the shape of calcite distribution curve almost followed that of the biofilm distribution (note that the scale of calcite volume fraction in Figure 4a is one-order magnitude smaller than that of biofilm volume fraction). Similar results were also given by the continuum-scale MICP modeling [Hommel et al., 2015b]. Figure 4b shows the distributions of REV-scale urea concentration in all three cases at the end of stage 2. The REV-scale concentration of a species in the water and biofilm was defined as $\bar{C} = \sum_{REV} V^0 (1 - \varepsilon^c) C / \sum_{REV} V^0 (1 - \varepsilon^c)$. The urea concentration and calcite distributions in case 2 indicated that the calcite precipitation was limited by the ureolysis rate in the presence of plenty of calcium ions. Under the condition of continuous injection of urea and calcium-rich medium, the biofilm distribution determined the distribution of calcite precipitation. Note that the time of two pore volumes of case 2 (i.e., 1.85 h) is much longer than that of the other two cases (i.e., 0.37 h). Therefore, we observed much more calcite precipitation throughout the domain in case 2.

To further study the effect of flow rate on calcite precipitation, we run three cases for the same time of 1.85 h at stage 2. Figure 4c shows the distributions of REV-scale calcite volume fraction in case 1, case 2, and case 3. In comparison, case 1 and case 3 gave more uniform distributions of calcite volume fraction, except there were much less calcite in the inlet region in either case. This is because of the low-pH medium injection (pH of 5.4). Case 2 gave a much lower amount of calcite precipitation. In addition, the distribution followed the biofilm distribution as mentioned in Figure 4a.

At stage 3, the system was closed for 4 h. Figure 4d shows the distributions of REV-scale biofilm volume fraction in all three cases at the end of stage 2 and stage 3. No obvious changes of biofilm distribution were found. This is because the endogenous decay and the decay due to calcite precipitation almost counteracted the growth of biofilm at stage 3. Figure 4e shows the distributions of REV-scale calcite volume fraction

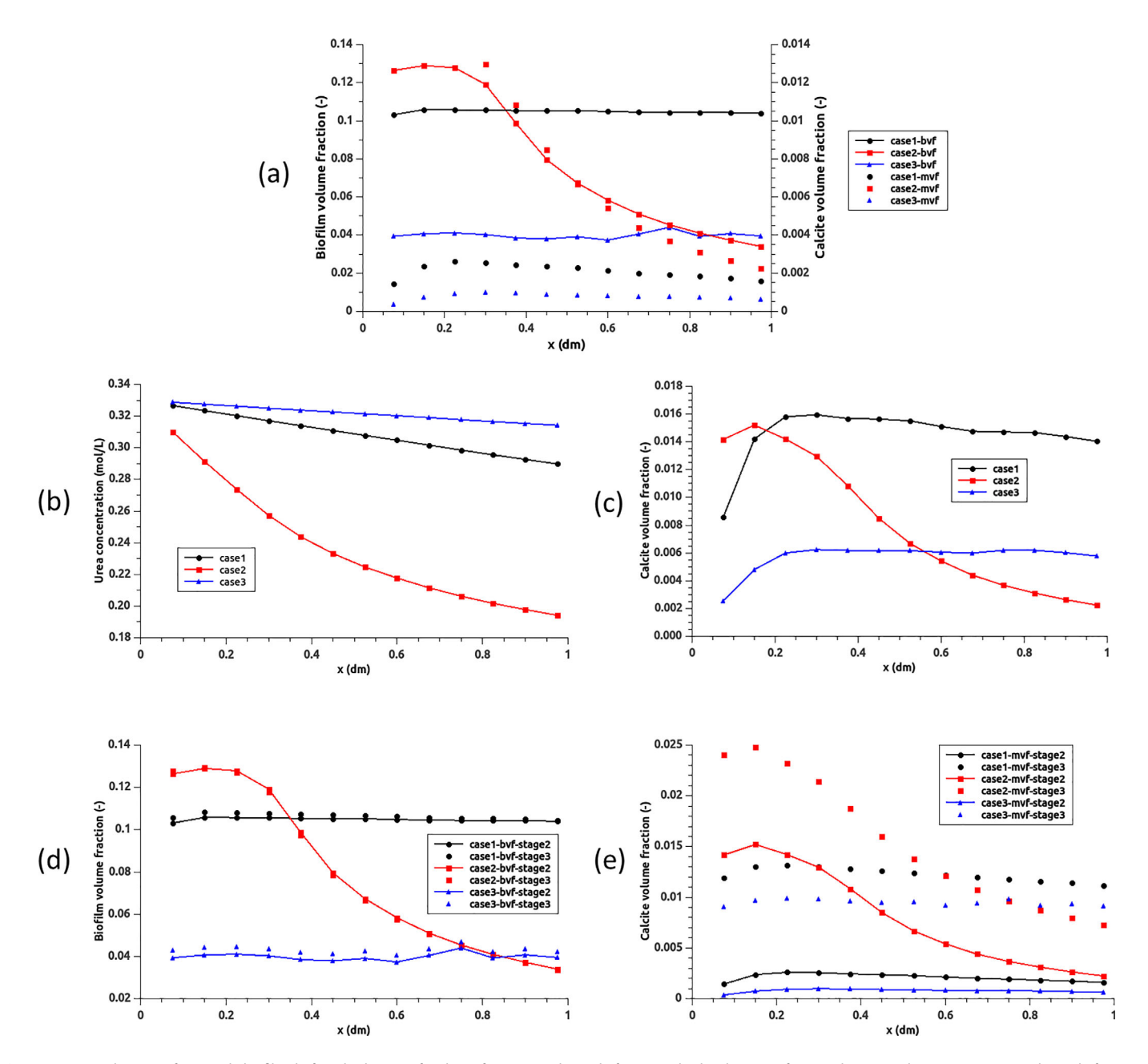


Figure 4. (a) Distributions of REV-scale biofilm (bvf) and calcite (mvf) volume fractions at the end of stage 2; (b) distributions of REV-scale urea molar concentration at the end of stage 2; (c) distributions of REV-scale calcite volume fraction after running all cases for 1.85 h at stage 2; (d) distributions of REV-scale biofilm volume fraction at the end of stage 2 and stage 3; (e) distributions of REV-scale calcite volume fraction at the end of stage 2 and stage 3.

at the end of stage 2 and stage 3. Because the calcite reaction rate was much larger than the diffusive rate of carbonate ions, the amount of precipitated calcite over stage 3 in each case was determined by the distribution of urea concentration at the end of stage 2. Therefore, the calcite distributions in case 1 and case 3 were still uniform along the flow direction at the end of stage 3. But, in case 2, the amount of precipitated calcite at stage 3 decreased along the flow direction, which was in accordance with the distribution of urea concentration at the end of stage 2 shown in Figure 4b.

4.2. Upscaling of Reaction Rates

To investigate the scaling effect on biogeochemical reaction rates, we defined the averaged reaction rate and the upscaled reaction rate (usually used in a continuum-scale model). First, the averaged biofilm growth rate (i.e., double-Monod kinetics of equation (6)) was calculated with the obtained pore-scale results as

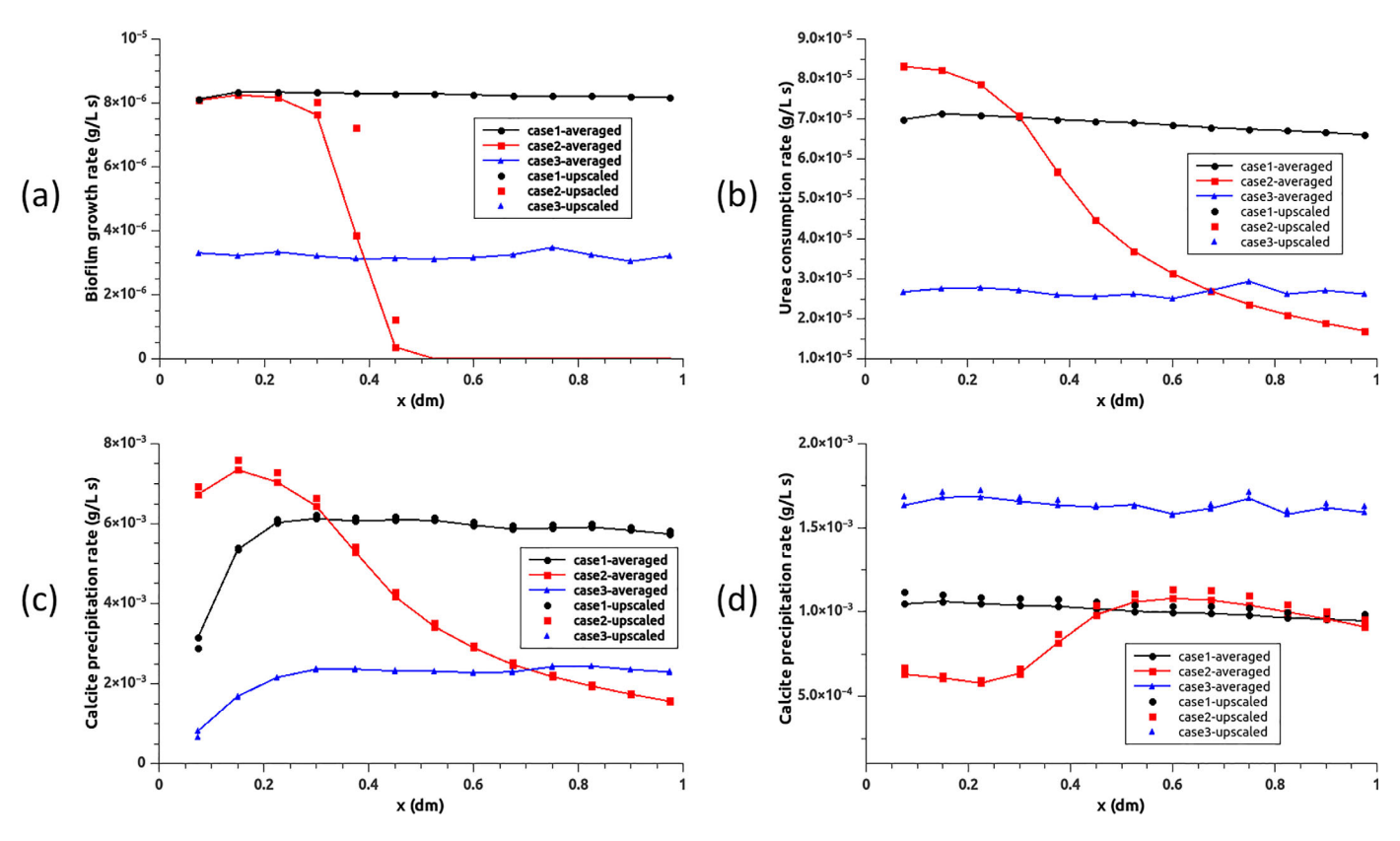


Figure 5. (a) Distributions of the averaged and upscaled biofilm growth rates along the flow direction at the end of stage 1; (b) distributions of the averaged and upscaled urea consumption rates along the flow direction at the end of stage 2; (c) distributions of the averaged and upscaled calcite precipitation rates along the flow direction at the end of stage 2; (d) distributions of the averaged and upscaled calcite precipitation rates along the flow direction in the middle of stage 3.

$$R_f^{ave} = \frac{\sum_{REV} k_{\mu} V^0 \varepsilon^f \rho^f \frac{C^n}{K_n + C^n} \frac{C^o}{K_o + C^o}}{\sum_{REV} V^0},$$
(14)

where the summation is over all pore elements in the REV; here the pore-element indices i and ij are omitted. Also, R_f^{ave} is called the "true" REV-scale reaction rate [Li et al., 2006]. We assumed that the microscale form of reaction kinetics was kept at the REV scale but in terms of averaged concentrations. Then, the upscaled biofilm growth rate was given as

$$R_f^{ups} = k_{\mu} \bar{\varepsilon}^f \rho^f \frac{\bar{C}^n}{K_n + \bar{C}^n} \frac{\bar{C}^o}{K_o + \bar{C}^o}, \tag{15}$$

where \bar{C} and $\bar{\epsilon}^f$ are the averaged (i.e., REV scale) concentration and averaged biofilm volume fraction. The difference between the two reaction rates shows the scaling effect. It is worth noting that in convention an upscaled quantity like R_f^{ups} should be experimentally measurable. Figure 5a shows the distributions of the averaged and upscaled biofilm growth rates along the flow direction at the end of stage 1. In case 1 and case 3, much larger concentrations of substrate and oxygen, compared to their half saturation constants, prevailed along the flow domain. For instance, in case 1, at the outlet the oxygen concentration was 1.7×10^{-3} g/L which was much larger than its half saturation constant of 2.0×10^{-5} g/L. Therefore, the biofilm growth rate at either the pore scale or the REV scale reduced to the zeroth order. This explains why there was no scaling effect for case 1 and case 3. In case 2, the biofilm growth rate varied from the zeroth order to the first order. There was strong scaling effect in the transitional zone (around x = 0.35 dm). The upscaled biofilm growth rate was overestimated. But, away from the transitional zone, the scaling effect was negligible.

Figure 5b shows the distributions of the averaged and upscaled urea consumption rates along the flow direction at the end of stage 2. The definition of the averaged and upscaled urea consumption rates is similar to that of the biofilm growth rates. Reexamining the form of the ureolysis kinetics (equation (11)) and the distributions of the urea molar concentration in Figure 4b, it is seen that the kinetics in all three cases could be approximated as the zeroth-order reaction. There was no transitional zone between the zeroth-order and first-order reactions. This explains why the scaling effect on the urea consumption rate was negligible.

The study of the scaling effect of calcite precipitation is somewhat complex. Again, we note that the upscaling here denotes the scaling from the pore-element scale to the REV scale. The scaling effect inside a pore element due to the mass transfer limitation (i.e., molecular diffusion) and complex nucleation mechanism [Noiriel et al., 2012] was simply accounted for by the correction coefficient, β . First, the "true" calcite precipitation rate was calculated as

$$r_{prec/diss}^{ave} = \frac{\sum_{REV} \beta \left(k_1 a^{H^+} + k_2 a^{H_2CO_3} + k_3 \right) \left(1 - \frac{a^{Ca^{2+}} a^{CO_3^{2-}}}{K_{sp}} \right)^{n_p} S^c}{\sum_{REV} V^0}.$$
 (16)

In the calculation of the upscaled precipitation rate, we first obtained the averaged geochemical component concentrations; then, the PHREEQC module was called to compute the averaged activities of proton, carbonate acid, calcium, and carbonate. This procedure is in accordance with laboratory measurements. The final form of the upscaled precipitation rate was given as

$$r_{prec/diss}^{ups} = \beta \left(k_1 \bar{a}^{H^+} + k_2 \bar{a}^{H_2CO_3} + k_3 \right) \left(1 - \frac{\bar{a}^{Ca^{2+}} \bar{a}^{CO_3^{2-}}}{K_{sp}} \right)^{n_p} \bar{S}^c, \tag{17}$$

where \bar{S}^c is the REV-scale specific area for calcite precipitation. Also, the correction coefficient β was assumed to be unchanged. Figure 5c shows the distributions of the averaged and upscaled calcite precipitation rates along the flow direction at the end of stage 2. Figure 5d shows the distributions of the averaged and upscaled calcite precipitation rates along the flow direction in the middle of stage 3. It is seen that there was no scaling effect in either the advection-dominant operation (stage 2) or the diffusion-dominant operation (stage 3). This is probably due to the fact that the injected calcium-rich medium had a very high concentration of calcium. As a result, the calcite precipitation was totally dominated by the ureolysis rate as discussed in Figure 4a. This explanation will be further confirmed in section 4.3. In Figure 5d, we can see that the calcite precipitation rate was smaller near the inlet in case 2. This is because the biofilm volume was larger there such that the calcium and carbonate ions were consumed faster; and the precipitation rate was much faster than the diffusion rate of carbonate ions. In the following, we further discuss why the heterogeneous distribution of biofilm had no scaling effect on the calcite precipitation in case 3. Figure 6 shows the pore-scale distributions of biofilm volume fraction, calcite volume fraction, pH value, and calcium concentration in the domain of 0.4 dm < x < 0.6 dm in case 3, in the middle of stage 3. It is seen that the calcite precipitation always followed the biofilm distribution at the pore scale. As a result, the pH values were relatively high around the biofilm due to the ammonium formation. Meanwhile, the calcium concentrations were a little bit low due to the consumption. But, by examining the three precipitation rate coefficients in equation (9), it was found that in MICP, due to alkaline conditions, the calcite precipitation rate was dominated by the third constant coefficient, k_3 . This means the precipitation rate is insensitive to the heterogeneity of pH field. Therefore, it explains why the heterogeneous distribution of biofilm had no scaling effect on the calcite precipitation. In comparison, in upscaling anorthite and kaolinite reaction rates relevant to geological CO₂ sequestration, there was very strong scaling effect with a heterogeneous distribution of reactive minerals [Li et al., 2006; Kim et al., 2011]. This is because those precipitation and dissolution rates were strongly dependent on the local pH values (acidic condition).

4.3. Simplification of the Geochemistry Calculation

In the MICP modeling, geochemistry calculations account for a large amount of computational efforts. If only calcite distribution is of interest, we may considerably simplify geochemical reactions. Also, from the previous analysis in this work, we found that the calcite precipitation rate was limited by the slow ureolysis

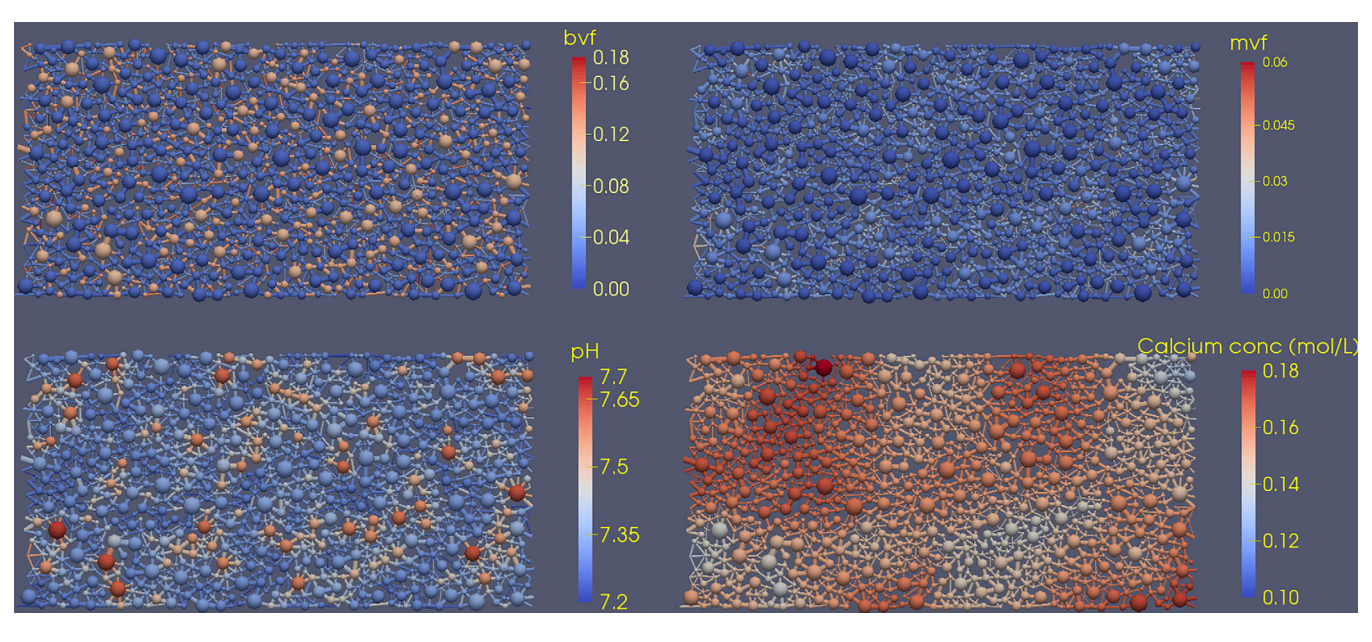


Figure 6. Pore-scale distributions of biofilm volume fraction (bvf), calcite volume fraction (mvf), pH value, and calcium concentration in the domain of 0.4 dm < x < 0.6 dm in case 3, in the middle of stage 3.

rate in the presence of rich calcium, which was the operating condition used in many other studies [Sham et al., 2013; Martinez et al., 2014; Hommel et al., 2015a, 2015b]. Then, the calcite precipitation rate may be approximated by

$$r_{prec/diss} = -R^{u} = -k_{urea}k_{ub}\rho^{f}\varepsilon^{f}\frac{m^{u}}{K_{u} + m^{u}}.$$
(18)

This way, the PHREEQC module was not used in the modeling. The transport of geochemical components was not modeled. This reduced the computational effort considerably. Figures 7a and 7b show the distributions of REV-scale calcite volume fraction in case 1 and case 2, at the end of stage 2 and at the end of stage 3, respectively. It is seen that the results of modeling without the geochemistry calculation were adequately accurate. Only small discrepancies were observed at the inlet region. This is because of the neglected low pH effect on the calcite precipitation at the inlet and the embedded mass equilibrium assumption of carbonate ions in the simplified model. After stage 3, the difference was negligible.

4.4. Local Mass Transfer Limitation

Due to the fast precipitation rate of calcite in a pore element, there may be strong mass transfer limitation of carbonate ions from biofilm to precipitation sites. But, if precipitation happens locally inside biofilm, the mass transfer limitation would be weak. Also, it depends on the pore size and biofilm distribution in a pore element. A mass transfer limitation of carbonate ions would induce local pH value variation. But, as mentioned above, the calcite precipitation is insensitive to the pH value under alkaline conditions. On the other hand, it is worth noting that a possible mass transfer limitation of carbonate ions had minor impact on the transport model of total carbon element in the pore-network model. This is because the species HCO_3^- accounts for the majority of carbon element.

Here we assumed three values (0.01, 0.1, and 1.0) of the correction coefficient β to investigate the effect of mass transfer limitation on the calcite precipitation. Figure 8a shows the distributions of REV-scale calcite volume fraction in case 1 at the end of stage 2 for three different correction coefficients. Only small differences in the calcite distribution between β =1.0 and 0.1 were found. This indicated that the calcite precipitation was still limited by the ureolysis rate. When the correction coefficient was further reduced to 0.01 (i.e., strong mass transfer limitation), the mass transfer rate of carbonate ions started to play a role in determining the precipitated amount of calcite. As a result, much less calcite precipitation was calculated. At stage 3, the system was closed. Obviously, over the whole stage, the precipitated calcite was determined only by

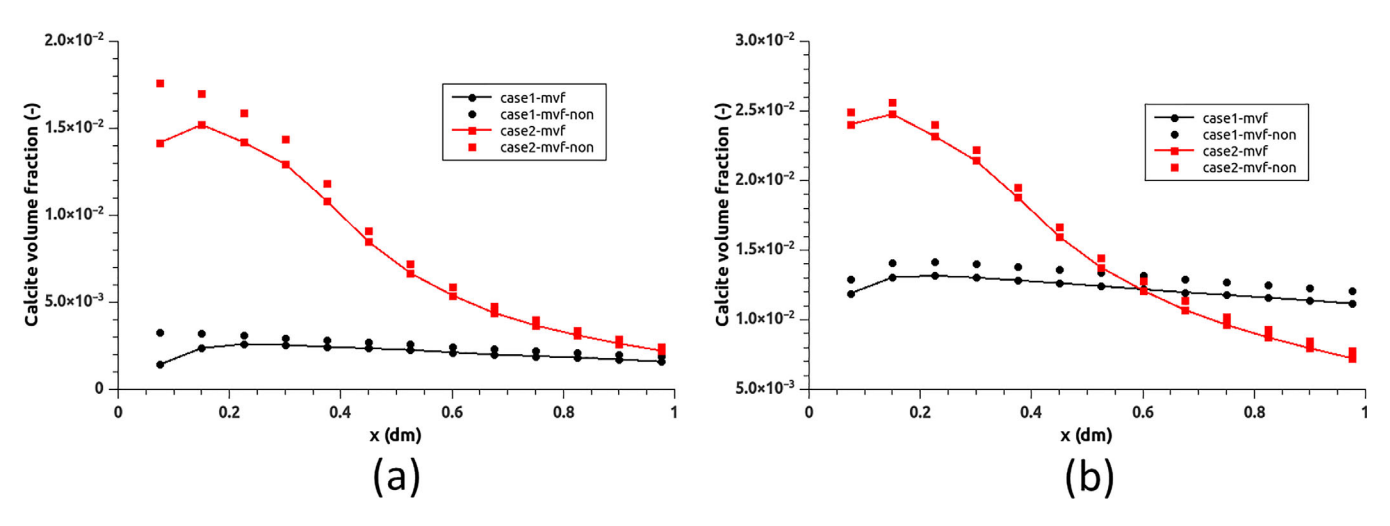


Figure 7. Distributions of REV-scale calcite volume fraction in case 1 and case 2 with (case1-mvf and case2-mvf) and without the geochemistry calculation (case1-mvf-non and case2-mvf) at the end of stage 2; and (b) at the end of stage 3.

the local urea concentration. Therefore, the mass transfer limitation had a negligible effect on calcite precipitation as shown in Figure 8b, which shows the temporal evolutions of the total calcite volume in case 1.

5. Conclusions and Outlook

In this research, we developed a pore-scale network model of MICP. Key parameters of biogeochemical reactions were obtained from the literature with experimental verifications. A typical three-stage (i.e., bio-film growth, injection of calcium-rich medium, and calcite precipitation) process was modeled to understand the pore-scale processes of MICP and the scale dependence of biogeochemical reaction rates. This can help us develop reliable and efficient field-scale models of MICP. Based on our study of three test cases by the pore-network modeling, we have drawn the following main conclusions.

In the stage of biofilm growth, more biofilm was observed in a pore throat compared to the surrounding pore bodies. This is because of the larger specific area of the pore throat resulting in more specific biomass attachment. Reducing the flow rate would cause the limitation of oxygen availability resulting in nonuniform distribution of biofilm along the flow direction. Then, in stage 2, i.e., injection of calcium-rich medium (similar to a continuous injection strategy in *Hommel et al.* [2015b]), the calcite precipitation was dependent on the biofilm distribution obtained from stage 1. This is because the calcite precipitation was limited by the ureolysis rate. Finally, in stage 3, the system was closed. The distribution of precipitated calcite was

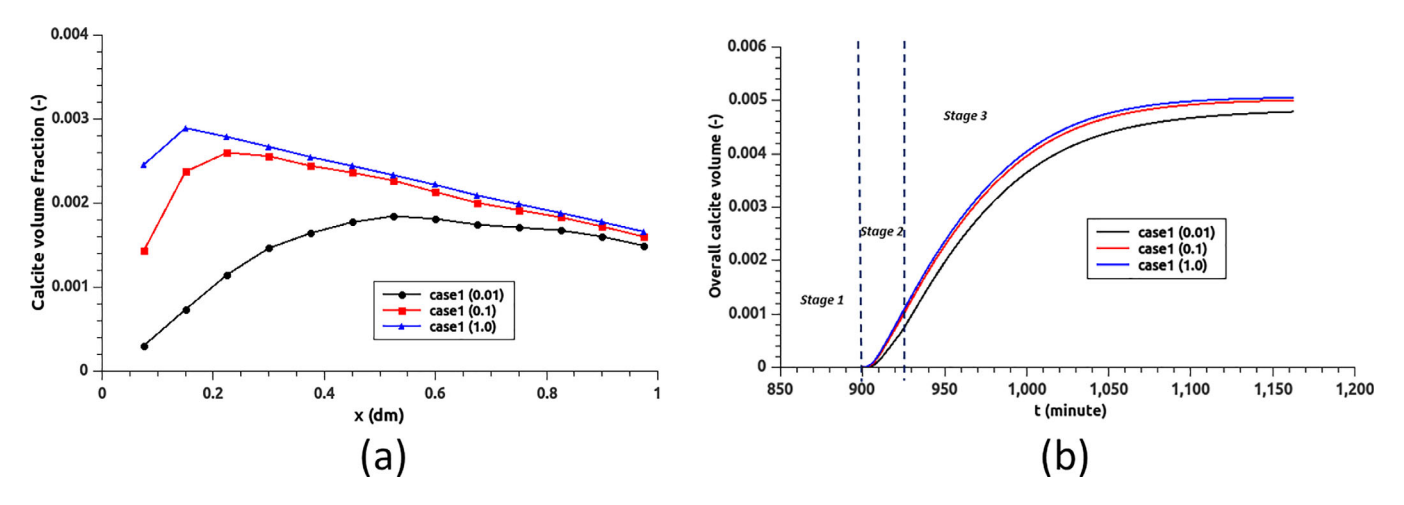


Figure 8. Under different mass transfer limitation conditions (β =0.01, 0.1, and 1.0), (a) distributions of REV-scale calcite volume fraction in case 1 at the end of stage 2; and (b) temporal evolutions of the total calcite volume in case 1.

determined by the distribution of urea concentration at the end of stage 2. This indicated that in a pulsed injection strategy, the distribution of precipitated calcite was not sensitive to the biofilm distribution. This would considerably simplify the development of MICP model. However, in a continuous injection strategy, the calcite distribution was determined by the biofilm distribution, which may cause severe clogging around an injection well.

In the study of scaling effect on biogeochemical reaction rates, it was found that under the operating conditions used in this work, there were negligible scaling effects on urea consumption rate, biofilm growth rate, and calcite precipitation rate. The only exception was that strong deviation between the averaged and upscaled biofilm growth rates was seen, when the biofilm growth rate varied from the zeroth order to first order in the averaged domain. However, notice that the transitional zone is very thin such that this scaling effect can be also neglected at the continuum scale. As a whole, no scaling effect may allow us to directly use the biogeochemical reaction rates measured from the lab.

Given the fact that the calcite precipitation rate was limited by the ureolysis rate in the presence of rich calcium ions, the calcite precipitation rate could be assumed to be stoichiometric to the ureolysis rate. This considerably reduced the computational effort. It was found that without severe mass transfer limitation of carbonate ions, similar modeling results of the calcite distribution were obtained without calculating the geochemical speciation.

Due to the local complexity of pore structure, biofilm and calcite distributions, there may be the mass transfer limitation of carbonate ions. We found that in stage 2 (similar to a continuous injection strategy), moderate mass transfer limitation had minor influence on the calcite precipitation. But, under severe limitation, much less calcite precipitation was predicted. In stage 3, the calcite precipitation was dominated by the local ureolysis rate. Therefore, the mass transfer limitation had negligible effect on the calcite distribution.

In future studies, the developed pore-network MICP model will be used to obtain the relationship between reduced porosity and permeability for the porous medium of interest. As mentioned in the beginning, this material property serves as an important input to a continuum-scale MICP model, and determines the performance of the MICP engineering. To this end, first, pore elements with complex geometries for representing a realistic porous medium need to be incorporated in the present pore-network model; second, direct simulations and micromodel experiments of the MICP need to be conducted for understanding the interaction between biofilm and calcite precipitation. This information will be also included in the pore-network model for predicting the relationship between reduced porosity and permeability.

Acknowledgments

This research was supported by the Dutch Technology Foundation STW, which is part of the Netherlands Organisation for Scientific Research (NOW) and which is partly funded by the Ministry of Economic Affairs. This research also has received funding from the European Research Council under the European Union's Seventh Framework Programme (FP/2007-2013)/ERC grant agreement 341225. Finally, we thank Johannes Hommel, Michael Afanasyev, Timo Heimovaara, Rainer Helmig, and Alfred B. Cunningham for the useful discussion. All data in this work are available upon request (chaozhong.gin@gmail.com).

References

- Acharya, R. C., A. J. Valocchi, C. J. Werth, and T. W. Willingham (2007), Pore-scale simulation of dispersion and reaction along a transverse mixing zone in two-dimensional porous media, *Water Resour. Res.*, 43, W10435, doi:10.1029/2007WR005969.
- Al Qabany, A., K. Soga, and C. Santamarina (2012), Factors affecting efficiency of microbially induced calcite precipitation, *J. Geotech. Geoenviron. Eng.*, 138(8), 992–1001, doi:10.1061/(ASCE)GT.1943-5606.0000666.
- Bachmeier, K. L., A. E. Williams, J. R. Warmington, and S. S. Bang (2002), Urease activity in microbiologically-induced calcite precipitation, J. Biotechnol., 93(2), 171–181, doi:10.1016/S0168-1656(01)00393-5.
- Barkouki, T. H., B. C. Martinez, B. M. Mortensen, T. S. Weathers, J. D. de Jong, T. R. Ginn, N. F. Spycher, R. W. Smith, and Y. Fujita (2011), Forward and inverse bio-geochemical modeling of microbially induced calcite precipitation in half-meter column experiments, *Transp. Porous Media*, 90(1), 23–39, doi:10.1007/s11242-011-9804-z.
- Bear, J., and Y. Bachmat (1991), Introduction to Modeling of Transport Phenomena in Porous Media, 16 pp., Kluwer Acad., Dordrecht, Netherlands.
- Brovelli, A., F. Malaguerra, and D. A. Barry (2009), Bioclogging in porous media: Model development and sensitivity to initial conditions, *Environ. Model. Software*, 24(5), 611–626, doi:10.1016/j.envsoft.2008.10.001.
- Charlton, S. R., and D. L. Parkhurst (2011), Modules based on the geochemical model PHREEQC for use in scripting and programming languages, *Comput. Geosci.*, 37(10), 1653–1663, doi:10.1016/j.cageo.2011.02.005.
- Cheng, L., R. Cord-Ruwisch, and M. A. Shahin (2013), Cementation of sand soil by microbially induced calcite precipitation at various degrees of saturation, *Can. Geotech. J., 50*(1), 81–90, doi:10.1139/cgj-2012-0023.
- Chou, L., R. M. Garrels, and R. Wollast (1989), Comparative study of the kinetics and mechanisms of dissolution of carbonate minerals, *Chem. Geol.*, 78(3–4), 269–282, doi:10.1016/0009-2541(89)90063-6.
- Cunningham, A. B., E. Lauchnor, J. Eldring, R. Esposito, A. C. Mitchell, A. Ebigbo, L. H. Spangler, R. Gerlach, and A. J. Phillips (2013), Abandoned well CO₂ leakage mitigation using biologically induced mineralization: Current progress and future directions, *Greenhouse Gases Sci. Technol.*, 3(1), 40–49, doi:10.1002/ghg.1331.
- Cunningham, A. B., A. J. Phillips, E. Troyer, E. Lauchnor, R. Hiebert, R. Gerlach, and L. Spangler (2014), Wellbore leakage mitigation using engineered biomineralization, *Energy Proc.*, 63, 4612–4619, doi:10.1016/j.egypro.2014.11.494.
- Cunningham, J. A., and I. Mendoza-Sanchez (2006), Equivalence of two models for biodegradation during contaminant transport in groundwater, *Water Resour. Res.*, 42, W02416, doi:10.1029/2005WR004205.

- Cuthbert, M. O., L. A. McMillan, S. Handley-Sidhu, M. S. Riley, D. J. Tobler, and V. R. Phoenix (2013), A field and modeling study of fractured rock permeability reduction using microbially induced calcite precipitation, *Environ. Sci. Technol.*, 47(23), 13,637–13,643, doi:10.1021/es402601a.
- De Muynck, W., K. Verbeken, N. De Belie, and W. Verstraete (2010a), Influence of urea and calcium dosage on the effectiveness of bacterially induced carbonate precipitation on limestone, *Ecol. Eng.*, 36(2), 99–111, doi:10.1016/j.ecoleng.2009.03.025.
- De Muynck, W., N. De Belie, and W. Verstraete (2010b), Microbial carbonate precipitation in construction materials: A review, *Ecol. Eng.*, 36(2), 118–136, doi:10.1016/j.ecoleng.2009.02.006.
- Deng, W., M. B. Cardenas, M. F. Kirk, S. J. Altman, and P. C. Bennett (2013), Effect of permeable biofilm on micro-and macro-scale flow and transport in bioclogged pores, *Environ. Sci. Technol.*, 47(19), 11,092–11,098, doi:10.1021/es402596v.
- Dhami, N. K., M. S. Reddy, and A. Mukherjee (2013), Biomineralization of calcium carbonates and their engineered applications: A review, Front. Microbiol., 4, 314, doi:10.3389/fmicb.2013.00314.
- Ebigbo, A., R. Helmig, A. B. Cunningham, H. Class, and R. Gerlach (2010), Modelling biofilm growth in the presence of carbon dioxide and water flow in the subsurface. *Adv. Water Resour.*, 33(7), 762–781. doi:10.1016/j.advwatres.2010.04.004.
- Ebigbo, A., A. Phillips, R. Gerlach, R. Helmig, A. B. Cunningham, H. Class, and L. H. Spangler (2012), Darcy-scale modeling of microbially induced carbonate mineral precipitation in sand columns, *Water Resources Research*, 48, W07519, doi:10.1029/2011WR011714.
- Fauriel, S., and L. Laloui (2012), A bio-chemo-hydro-mechanical model for microbially induced calcite precipitation in soils, *Comput. Geotech.*, 46, 104–120, doi:10.1016/j.compgeo.2012.05.017.
- Fujita, Y., J. L. Taylor, T. L. T. Gresham, M. E. Delwiche, F. S. Colwell, T. L. Mcling, L. M. Petzke, and R. W. Smith (2008), Stimulation of microbial urea hydrolysis in groundwater to enhance calcite precipitation, *Environ. Sci. Technol.*, 42(8), 3025–3032, doi:10.1021/es702643g.
- Hassanizadeh, S. M., and W. G. Gray (1990), Mechanics and thermodynamics of multiphase flow in porous media including interphase boundaries. *Adv. Water Resour.*, 13(4), 169–186. doi:10.1016/0309-1708(90)90040-B.
- Hommel, J., A. B. Cunningham, R. Helmig, A. Ebigbo, and H. Class (2013), Numerical investigation of microbially induced calcite precipitation as a leakage mitigation technology, *Energy Proc.*, 40, 392–397, doi:10.1016/j.egypro.2013.08.045.
- Hommel, J., E. Lauchnor, A. J. Phillips, R. Gerlach, A. B. Cunningham, R. Helmig, A. Ebigbo, and H. Class (2015a), A revised model for microbially induced calcite precipitation: Improvements and new insights based on recent experiments, *Water Resour. Res.*, 51(5), 3695–3715, doi:10.1002/2014WR016503.
- Hommel, J., E. Lauchnor, R. Gerlach, A. B. Cunningham, A. Ebigbo, R. Helmig, and H. Class (2015b), Investigating the influence of the initial biomass distribution and injection strategies on biofilm-mediated calcite precipitation in porous media, *Transp. Porous Media*, 114, 557, doi:10.1007/s11242-015-0617-3.
- Horn, H., H. Reiff, and E. Morgenroth (2003), Simulation of growth and detachment in biofilm systems under defined hydrodynamic conditions, *Biotechnol. Bioenq.*, 81(5), 607–617, doi:10.1002/bit.10503.
- Ivanov, V., and J. Chu (2008), Applications of microorganisms to geotechnical engineering for bioclogging and biocementation of soil in situ, Rev. Environ. Sci. Biotechnol., 7(2), 139–153, doi:10.1007/s11157-007-9126-3.
- Kang, Q., P. C. Lichtner, H. S. Viswanathan, and A. I. Abdel-Fattah (2010), Pore scale modeling of reactive transport involved in geologic CO₂ sequestration, *Transp.Porous Media*, 82(1), 197–213, doi:10.1007/s11242-009-9443-9.
- Kim, D., C. A. Peters, and W. B. Lindquist (2011), Upscaling geochemical reaction rates accompanying acidic CO₂-saturated brine flow in sandstone aquifers, *Water Resour. Res.*, 47, W01505, doi:10.1029/2010WR009472.
- Kim, D. S., and H. S. Fogler (2000), Biomass evolution in porous media and its effects on permeability under starvation conditions, *Biotechnol. Bioeng.*, 69(1), 47–56, doi:10.1002/(SICI)1097-0290(20000705)69:1 < 47::AID-BIT6 > 3.0.CO;2-N.
- Lauchnor, E. G., L. N. Schultz, S. Bugni, A. C. Mitchell, A. B. Cunningham, and R. Gerlach (2013), Bacterially induced calcium carbonate precipitation and strontium coprecipitation in a porous media flow system, *Environ. Sci. Technol.*, 47(3), 1557–1564, doi:10.1021/es304240y.
- Lauchnor, E. G., D. M. Topp, A. E. Parker, and R. Gerlach (2015), Whole cell kinetics of ureolysis by Sporosarcina pasteurii, J. Appl. Microbiol., 118(6), 1321–1332, doi:10.1111/jam.12804.
- Li, L., C. A. Peters, and M. A. Celia (2006), Upscaling geochemical reaction rates using pore-scale network modeling, *Adv. Water Resour.*, 29(9), 1351–1370, doi:10.1016/j.advwatres.2005.10.011.
- Li, L., C. A. Peters, and M. A. Celia (2007), Reply to "Comment on upscaling geochemical reaction rates using pore-scale network modeling" by Peter C. Lichtner and Qinjun Kang, Adv. Water Resour., 30(3), 691–695, doi:10.1016/j.advwatres.2006.05.002.
- Lichtner, P. C., and Q. Kang (2007), Upscaling pore-scale reactive transport equations using a multiscale continuum formulation, *Water Resour. Res.*, 43, W12S15, doi:10.1029/2006WR005664.
- Martinez, B. C., J. T. DeJong, and T. R. Ginn (2014), Bio-geochemical reactive transport modeling of microbial induced calcite precipitation to predict the treatment of sand in one-dimensional flow, Comput. Geotech., 58, 1–13, doi:10.1016/j.compgeo.2014.01.013.
- Mitchell, A. C., A. Phillips, L. Schultz, S. Parks, L. Spangler, A. B. Cunningham, and R. Gerlach (2013), Microbial CaCO₃ mineral formation and stability in an experimentally simulated high pressure saline aquifer with supercritical CO₂, Int. J. Greenhouse Gas Control, 15, 86–96, doi: 10.1016/j.ijggc.2013.02.001.
- Nogues, J. P., J. P. Fitts, M. A. Celia, and C. A. Peters (2013), Permeability evolution due to dissolution and precipitation of carbonates using reactive transport modeling in pore networks, *Water Resour. Res.*, 49, 6006–6021, doi:10.1002/wrcr.20486.
- Noiriel, C., C. I. Steefel, L. Yang, and J. Ajo-Franklin (2012), Upscaling calcium carbonate precipitation rates from pore to continuum scale, *Chem. Geol.*, 318–319, 60–74, doi:10.1016/j.chemgeo.2012.05.014.
- Noiriel, C., C. I. Steefel, L. Yang, and D. Bernard (2015), Effects of pore-scale precipitation on permeability and flow, *Adv. Water Resour.*, 95, 125–137, doi:10.1016/j.advwatres.2015.11.013.
- Parkhurst, D. L., and C. A. J. Appelo (2013), Description of input and examples for PHREEQC version 3—A computer program for speciation, batch-reaction, one-dimensional transport, and inverse geochemical calculations, *U.S. Geol. Surv. Tech. Methods, Book 6, Chap. A43*, 497 pp. [Available at http://pubs.usgs.gov/tm/06/a43.]
- Peszynska, M., A. Trykozko, G. Iltis, S. Schlueter, and D. Wildenschild (2015), Biofilm growth in porous media: Experiments, computational modeling at the porescale, and upscaling, *Adv. Water Resour.*, 95, 288–301, doi:10.1016/j.advwatres.2015.07.008.
- Phillips, A. J., R. Gerlach, E. Lauchnor, A. C. Mitchell, A. B. Cunningham, and L. Spangler (2013), Engineered applications of ureolytic biomineralization: A review, *Biofouling*, 29(6), 715–733, doi:10.1080/08927014.2013.796550.
- Phillips, A. J., J. Eldring, R. Hiebert, E. Lauchnor, A. C. Mitchell, A. Cunningham, L. Spangler, and R. Gerlach (2015), Design of a meso-scale high pressure vessel for the laboratory examination of biogeochemical subsurface processes, *J. Pet. Sci. Eng.*, 126, 55–62, doi:10.1016/j.petrol.2014.12.008.
- Phillips, A. J. et al. (2016), Fracture sealing with microbially-induced calcium carbonate precipitation: A field study, *Environ. Sci. Technol.*, 50(7), 4111–4117, doi:10.1021/acs.est.5b05559.

1944/973, 2016, 11, Downloaded from https://agupubs.onlinelibrary.wiley.com/doi/10.1002/2016WR019128 by Chao-Zhong Qin , Wiley Online Library on [21/10/2023]. See the Terms and Conditions (https://onlinelibrary.wiley.com/terms

- Pintelon, T. R. R., C. Picioreanu, M. C. M. van Loosdrecht, and M. L. Johns (2012), The effect of biofilm permeability on bio-clogging of porous media, *Biotechnol. Bioeng.*, 109(4), 1031–1042, doi:10.1002/bit.24381.
- Qin, C. (2015), Water transport in the gas diffusion layer of a polymer electrolyte fuel cell: Dynamic pore-network modeling, *J. Electrochem. Soc.*, 162(9), F1036–F1046, doi:10.1149/2.0861509jes.
- Qin, C. Z., and S. M. Hassanizadeh (2014), Multiphase flow through multilayers of thin porous media: General balance equations and constitutive relationships for a solid-gas-liquid three-phase system, *Int. J. Heat Mass Transfer*, 70, 693–708, doi:10.1016/j.ijheatmasstransfer.
- Qin, C. Z., and S. M. Hassanizadeh (2015a), Solute mass exchange between water phase and biofilm for a single pore, *Transp. Porous Media*, 109(2), 255–278, doi:10.1007/s11242-015-0513-x.
- Qin, C.-Z., and S. M. Hassanizadeh (2015b), Pore-network modeling of solute transport and biofilm growth in porous media, *Transp. Porous Media*, 110(3), 345–367, doi:10.1007/s11242-015-0546-1.
- Raoof, A., and S. Majid Hassanizadeh (2010), A new method for generating pore-network models of porous media, *Transport Porous Media*, 81, 391–407, doi:10.1007/s11242-009-9412-3.
- Raoof, A., H. M. Nick, T. K. T. Wolterbeek, and C. J. Spiers (2012), Pore-scale modeling of reactive transport in wellbore cement under CO₂ storage conditions. *Int. J. Greenhouse Gas Control.* 11, supplement. 67–77, doi:10.1016/j.ijagc.2012.09.012.
- Rosenzweig, R., A. Furman, C. Dosoretz, and U. Shavit (2014), Modeling biofilm dynamics and hydraulic properties in variably saturated soils using a channel network model, *Water Resour. Res.*, 50, 5678–5697, doi:10.1002/2013WR015211.
- Sham, E., M. D. Mantle, J. Mitchell, D. J. Tobler, V. R. Phoenix, and M. L. Johns (2013), Monitoring bacterially induced calcite precipitation in porous media using magnetic resonance imaging and flow measurements, *J. Contam. Hydrol.*, 152, 35–43, doi:10.1016/j.jconhyd.2013.
- Steefel, C., D. Depaolo, and P. Lichtner (2005), Reactive transport modeling: An essential tool and a new research approach for the Earth sciences. *Earth Planet. Sci. Lett.*, 240(3–4), 539–558, doi:10.1016/j.epsl.2005.09.017.
- Tang, Y., A. J. Valocchi, C. J. Werth, and H. Liu (2013), An improved pore-scale biofilm model and comparison with a microfluidic flow cell experiment, *Water Resour. Res.*, 49, 8370–8382, doi:10.1002/2013WR013843.
- Thullner, M., and P. Baveye (2008), Computational pore network modeling of the influence of biofilm permeability on bioclogging in porous media, *Biotechnol. Bioeng.*, 99(6), 1337–1351, doi:10.1002/bit.21708.
- Van Noorden, T. L., I. S. Pop, A. Ebigbo, and R. Helmig (2010), An upscaled model for biofilm growth in a thin strip, Water Resour. Res., 46, W06505. doi:10.1029/2009WR008217.
- Von Der Schulenburg, D. A. G., T. R. R. Pintelon, C. Picioreanu, M. C. M. Van Loosdrecht, and M. L. Johns (2009), Three-dimensional simulations of biofilm growth in porous media, AIChE J., 55(2), 494–504, doi:10.1002/aic.11674.
- Yoon, H., A. J. Valocchi, C. J. Werth, and T. Dewers (2012), Pore-scale simulation of mixing-induced calcium carbonate precipitation and dissolution in a microfluidic pore network, *Water Resour. Res.*, 48, W02524, doi:10.1029/2011WR011192.
- Zhang, C., K. Dehoff, N. Hess, M. Oostrom, T. W. Wietsma, A. J. Valocchi, B. W. Fouke, and C. J. Werth (2010), Pore-scale study of transverse mixing induced CaCO₃ precipitation and permeability reduction in a model subsurface sedimentary system, *Environ. Sci. Technol.*, 44(20), 7833–7838. doi:10.1021/es1019788.
- Zhang, T., and I. Klapper (2010), Mathematical model of biofilm induced calcite precipitation, Water Sci. Technol., 61(11), 2957–2964, doi: 10.2166/wst.2010.064.
- Zhang, T., and I. Klapper (2014), Critical occlusion via biofilm induced calcite precipitation in porous media, *New J. Phys.*, *16*, 55009, doi: 10.1088/1367-2630/16/5/055009.
- Zhou, J. C. (2015), Modeling MIC and metal precipitation with a 1D reactive transport model, MS thesis, Dep. of Geosci. and Eng., Delft Univ. of Technol., Delft, Netherlands.

use; OA

governed by the applicable Creative Commons